Depth slicing of multi-receiver EMI measurements to enhance the delineation of contrasting subsoil features

Timothy Saey [a,*], Philippe De Smedt [a], Mohammad Monirul Islam [a], Eef Meerschman [a], Ellen Van De Vijver [a], Alexander Lehouck [b,c], Marc Van Meirvenne [a]

[a] Research Group Soil Spatial Inventory Techniques, Faculty of Bioscience Engineering, Ghent University, Coupure 653, 9000 Gent, Belgium
[b] Abdijmuseum Ten Duinen 1138, Koninklijke Prinslaan 6-8, 8670 Koksijde , Belgium
[c] Department of Medieval History, Faculty of Arts and Philosophy, Sint-Pietersnieuwstraat 35, 9000 Gent, Belgium

ARTICLE INFO

ABSTRACT

Mobile multi-receiver electromagnetic induction sensors provide simultaneous readings of the apparent electrical conductivity (ECa) from overlapping soil volumes. Therefore, small contrasting features can be difficult to identify because they have a limited contribution to the bulk measurement, especially if they are present in the subsoil (i.e. beneath the topsoil). Integrating ECa data from simultaneous measurements with multiple coil configurations has the potential to elucidate the variability within the soil profile as it enables modelling the electrical conductivity (EC) for distinct depth intervals. Therefore, it was our objective to develop a methodology to enhance the delineation of contrasting subsoil features, such as in-filled gullies and archaeological features. We selected a 3.5 ha study site where contrasting features were expected. A three-layered build-up was taken as the initial EC-slicing model. After varying the interface depths, the shallowest and deepest EC-depth slice showed a clear minimum of their combined variances at interface depths of 0.36 m, which corresponded to the ploughing depth, and 0.86 m. This implies that the EC-depth slice in-between these depths, contained a demonstrably higher variability. A sub-area of 0.85 ha was completely excavated to a depth of 0.7 m, revealing the subsoil features and the host material. An automated edge detection algorithm showed that the EC-depth slice was superior to any individual ECa measurement for delineating the contrasting subsoil features. Therefore, we concluded that depth slicing by integrating simultaneous ECa signals from a multi-receiver EMI sensor clearly improved the identification of subsoil features.

1. Introduction

Electromagnetic induction (EMI) is considered very suitable to map the subsoil variability because of its ability to map the apparent electrical conductivity (ECa), which in a non-saline soil is essentially controlled by soil texture and water content (Saey et al., 2009b). ECa can be defined as the depth weighted average of the electric conductivity of a column of material to a specific depth, expressed in milliSiemens per metre (mS m^{-1}). Although useful for investigating the lateral spatial soil variation, the measured ECa provides limited information on how conductivity varies vertically because the relationship between a specific soil and a particular ECa reading is not straightforward (Corwin and Lesch, 2005).

Advanced EMI instruments increasingly provide comprehensive data sets that can be used to quantify the subsoil variability (Pellerin and Wannamaker, 2005). The depth of penetration of the electromagnetic signal is influenced by the instrument's coil orientation, the coil separation and the measurement frequency. Therefore, data from multi-frequency (Brosten et al., 2011; Tromp-Van Meerveld and McDonnell, 2009) and multi-receiver (Monteiro Santos et al., 2010; Saey et al., 2009a) instruments increase the possibilities to infer depth variations in soil properties. Brosten et al. (2011) produced a three-dimensional EC-volume from multi-frequency ECa data. These inverted EC models show changes in lateral and vertical EC distribution. With multi-receiver instruments, the use of multiple configurations improves the possibilities of identifying different subsoil features. This leads to a better interpretation (Saey et al., 2011b) for a variety of applications like precision agriculture (Vitharana et al., 2008), archaeology (Saey et al., 2011a), groundwater resource evaluation (Brosten et al., 2011), contaminant distribution mapping (Lee et al., 2006; Martinelli et al., 2012) and vadose zone hydrology (Robinson et al., 2012). Measurements with these multi-receiver EMI instruments can be inverted to provide quantitative electrical conductivity estimates as a function of depth. Monteiro Santos et al. (2010) inverted multi-receiver ECa data collected with a DUALEM-421S instrument using a smooth inversion algorithm, to construct a global image of the subsurface distribution of EC and therefore to discern changes with depth. Combining multiple signals

---

* Corresponding author.
E-mail address: Timothy.Saey@UGent.be (T. Saey).

of a multi-receiver EMI proximal soil sensor implies measuring the ECa of overlapping soil volumes (Beamish, 2011), because the different coil configurations provide simultaneous measurements with different depth sensitivity (Saey et al., 2009a). Therefore, small contrasting features can be difficult to identify because they have a limited contribution to the bulk measurement, especially if they are only present in the subsoil. The integration of the simultaneous measurements has the potential to improve the discrimination of these small features by modelling the conductivity in-between distinct depth intervals.

The objective of this research was to improve the delineation of contrasting subsoil features within different soil layers. By integrating the multiple ECa measurements of a multi-receiver EMI sensor, the layer with the highest conductivity contrast is to be identified by varying its interface depths. This way, the potential to discriminate between the contrasting soil features within this layer should be enhanced. Furthermore, an edge detection algorithm will be applied to evaluate the straightforwardness of the model for delineating subsoil features in the depth slices.

2. Site description

The study site that we selected was a 3.5 ha agricultural field that was intensely occupied during medieval times (Lehouck, 2010). The study site is located in the western part of the Belgian coastal plain (central coordinates: 51°06′39″N and 2°41′55″E) (Fig. 1).

Throughout the entire study area, soil characteristics are rather uniform. Tertiary deposits form the sandy substrate (C2) and are overlain with Quaternary and Holocene deposits forming a ploughed clayey A-horizon (A) and a largely unaltered C1 layer (Vandenbohede and Lebbe, 2011). The current microrelief in this area results from both natural and man-induced processes (Baeteman, 1991; Ervynck et al., 1999). The site was surveyed with an EMI proximal soil sensor to map the archaeological landscape prior to the conversion into a larger golf terrain.

3. Electromagnetic induction instrument

EMI instruments use a transmitter coil (Tx) and one or more receiving coils (Rx) to measure the EM field coupling in the affected medium. For applications in mapping the soil variability, they typically operate at small Tx–Rx separations and at low frequency (e.g. <15 kHz). The combined separation-frequency EM attribute is designed to provide a measure of the subsoil conductivity across a depth scale that is determined by the Tx–Rx separation and the coil orientations used (Beamish, 2011). The DUALEM-21S electromagnetic induction sensor, used in this study, consists of one transmitter and four receiver coils. These four receiver coils are located at spacings of 1, 1.1, 2 and 2.1 m from the transmitter. The 1 m and 2 m transmitter-receiver pairs are in a horizontal coplanar coil mode (respectively HCP,1 and HCP,2), while the 1.1 m and 2.1 m pairs are placed in a perpendicular coil mode (respectively PERP,1 and PERP,2). McNeill (1980) approximated the Maxwell's equations describing the depth sensitivity of each coil configuration by analytical equations defined by the cumulative response from the soil volume above a depth Z (in m) for the horizontal coplanar dipole mode ($R_{HCP}(Z)$). Dualem Inc (2007) developed the equation of the cumulative response for the perpendicular dipole mode ($R_{PERP}(Z)$) based on Wait (1962):

$$R_{\mathrm{HCP},X}(Z) = 1 - \left(4 \cdot \frac{Z^2}{X^2} + 1\right)^{-0.5} \tag{1}$$

$$R_{\mathrm{PERP},X}(Z) = 2\frac{Z^2}{X^2}\left(4 \cdot \frac{Z^2}{X^2} + 1\right)^{-0.5} \tag{2}$$
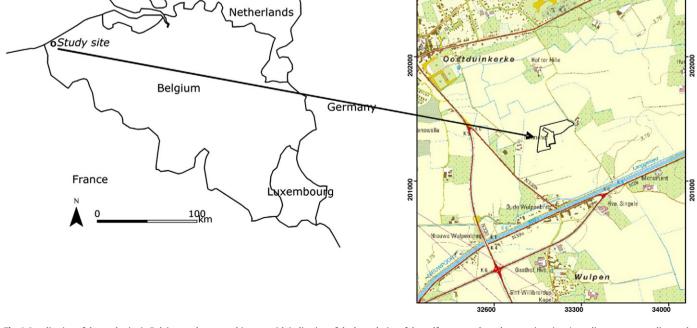

Fig. 1. Localisation of the study site in Belgium and topographic map with indication of the boundaries of the golf court, study and excavation sites (coordinates are according to the Belgian metric Lambert 72 projection).

with X being the transmitter-receiver spacing, and both $R_{HCP}(Z)$ and $R_{PERP}(Z)$ are expressed as percentage of the measured signal, relative to 1.

The depth of exploration (DOE) differs for the different coil configurations as follows: PERP,1 = 0.5 m, PERP,2 = 1.0 m, HCP,1 = 1.6 m and HCP,2 = 3.2 m. These are the depths at which 70% of the measured response of the coil configuration is attributed to the soil volume from the soil surface up to these depths. So 30% of the response originates from soil material below the DOE.

4. ECa survey

The study site was surveyed with the DUALEM-21S EMI instrument. Measurements were performed at 1.7 m apart parallel lines, and approximately 5 measurements were logged within a 1 m track. Measurements of each particular coil configuration were performed simultaneously. Ordinary point kriging (Goovaerts, 1997) was then used to interpolate these data to a 0.5 by 0.5 m grid. This geostatistical technique ensures unbiased estimates with minimal estimation variance. Moreover, kriging includes declustering the sensor data, which accounts for the denser within-line measurements (0.2 m). Ordinary kriging weights are derived from a variogram, which is a model of the spatial structure (Goovaerts, 1997; Webster and Oliver, 2007).

We modelled the variograms by manually fitting a variogram model to the data. A maximum of 64 neighbours was used within a circular search area around the location being interpolated. The variograms models are shown in Fig. 2. The ECa of the HCP coil configurations proves to contain a larger spatial structure than the ECa of the PERP coil configurations. Moreover, the larger the DOI, the smaller the nugget effect or random noise.

Table 1 shows the descriptive statistics of the four ECa measurements taken at the study site. The increase of the average ECa with increasing DOE, i.e. from the PERP,1 to the PERP,2 up to the HCP,1 coil configurations, implies an elevated soil EC in the top 1.5 m. Below this depth, EC does not increase, indicating constant soil characteristics such as soil texture and soil moisture content. Furthermore, the high maximum value of $ECa_{PERP,1}$ and the negative minimum values from all coil configurations indicated the presence of metal objects in the topsoil (Saey et al., 2011b). Fig. 3 shows the four ECa maps of the study site. Here, different linear and meandering features were observed across the study site and analogue patterns can be seen in all measurements. The clear distinction between these features is caused by a large EC contrast between the clayey topsoil and the underlying sand. This enhances the discrimination potential of the filled-in ditches and gullies (De Smedt et al., 2012).
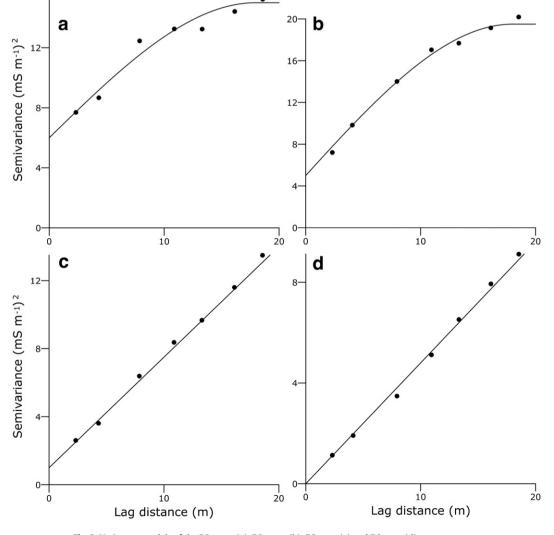

Fig. 2. Variogram models of the $ECa_{PERP,1}$ (a), $ECa_{PERP,2}$ (b), $ECa_{HCP,1}$ (c) and $ECa_{HCP,2}$ (d) measurements.

Variable	DOE	*m*	min	max	std
ECa$_{PERP,1}$	0.5	21	−32	133	5.3
ECa$_{PERP,2}$	1.0	27	−15	54	6.1
ECa$_{HCP,1}$	1.6	32	−53	58	5.6
ECa$_{HCP,2}$	3.2	33	−9	59	5.4

5. EC-depth modelling

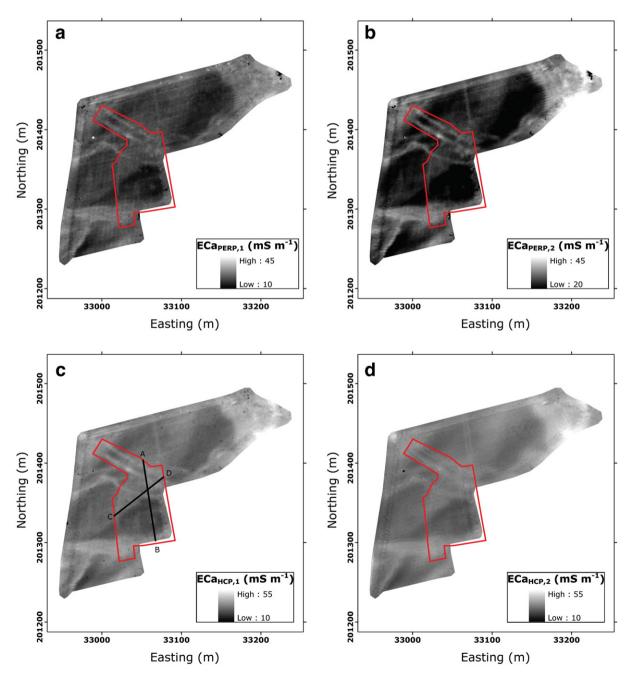In a layered-soil model, the relative contribution of all material up to a depth *Z* below the EMI sensor to the measured ECa is given by Eqs. (1) and (2) for both HCP and PERP coil configurations. Taking these definitions into account, the response of an *N*-layered soil is calculated by adding the contributions from each layer independently, weighted according to their EC and *Z* (Saey et al., 2009a):

$$ECa = R(Z_1)\cdot EC_1^* + \sum_{j=2}^{N-1}\left[R(Z_j)-R(Z_{j-1})\right]\cdot EC_j^* + [1-R(Z_{N-1})]\cdot EC_N^* \quad (3)$$

A combination of these equations enables to invert the ECa data, whereas the modelled EC can be discerned within discrete depth intervals. Since the DUALEM-21S sensor measures the ECa simultaneously with four different coil configurations, we can assume a three-layered soil model where the layers have a constant thickness. From this, a set of four equations with five unknown parameters can be derived. This allows to invert the simultaneous ECa measurements to obtain the EC* of

Fig. 3. ECa$_{PERP,1}$ (a), ECa$_{PERP,2}$ (b), ECa$_{HCP,1}$ (c) and ECa$_{HCP,2}$ (d) measurements (converted to a reference temperature of 25 °C) with localisation of the excavated site (polygon) and transects AB and CD.

the shallow (EC_1^*), middle (EC_2^*) and deeper (EC_3^*) soil layers with interface boundaries at Z_1 and Z_2. Z_1 is the depth of the boundary between the shallow and middle soil layers and Z_2 is the depth of the interface between the middle and deeper soil layers.

The following set of equations was defined, taking the height of the DUALEM-21S sensor above the soil surface (Z_s) into account:

$$\mathrm{ECa}_{\mathrm{PERP},X} = \left[R_{\mathrm{PERP},X}(Z_1 + Z_s) - R_{\mathrm{PERP},X}(Z_s) \right] \cdot \mathrm{EC}_1^* + \left[R_{\mathrm{PERP},X}(Z_2 + Z_s) \right.$$
$$\left. - R_{\mathrm{PERP},X}(Z_1 + Z_s) \right] \cdot \mathrm{EC}_2^* + \left[1 - R_{\mathrm{PERP},X}(Z_2 + Z_s) \right] \cdot \mathrm{EC}_3^* \tag{4}$$

$$\mathrm{ECa}_{\mathrm{HCP},X} = \left[R_{\mathrm{HCP},X}(Z_1 + Z_s) - R_{\mathrm{HCP},X}(Z_s) \right] \cdot \mathrm{EC}_1^* + \left[R_{\mathrm{HCP},X}(Z_2 + Z_s) \right.$$
$$\left. - R_{\mathrm{HCP},X}(Z_1 + Z_s) \right] \cdot \mathrm{EC}_2^* + \left[1 - R_{\mathrm{HCP},X}(Z_2 + Z_s) \right] \cdot \mathrm{EC}_3^* \tag{5}$$

with $R_{\mathrm{PERP},X}(Z)$ and $R_{\mathrm{HCP},X}(Z)$ the cumulative responses above a depth Z for the PERP and HCP mode and transmitter-receiver coil spacing X (either 1 m or 2 m).

To focus on the contrasting subsoil features on our study site, we aimed at improving the contrast between the features and the background value of one layer with a fixed thickness. We aimed at developing a filter that amplifies the maximum horizontal conductivity gradient. Therefore, the interface depth Z_1 was varied to account for the layer(s) with the highest conductivity contrast. This was done for a range of Z_1 values going from 0.1 to 2 m with a step interval of 0.2 m. Because the DOEs of both the PERP,1 and PERP,2 coil configurations and the PERP,2 and HCP,1 coil configurations differ by 0.5 m, Z_2 was taken as $Z_1 + 0.5$ m. Subsequently, EC_1^*, EC_2^* and EC_3^* were calculated across 2 transects (AB and CD, Fig. 3c) by solving the set of 4 equations using the Levenberg–Marquardt algorithm (Marquardt, 1963) at each measurement point of the transect. The variances of EC_1^*, EC_2^* and EC_3^* were calculated for the range of Z_1 values across both transects and compared to obtain an optimal value of Z_1. We aimed at minimising the variances of both EC_1^* and EC_3^* or maximising the variance of EC_2^*, because the subsoil features were assumed to be located below the topsoil, within this simulated soil layer. An optimum value for Z_1 was found for both EC_1^* and EC_3^* as their multiplied total variances $\sigma_{EC_1^*} \times \sigma_{EC_3^*}$ across both transects showed a clear minimum. The optimum Z_1 was found at 0.36 m (Fig. 4), which corresponds to the depth of the plough layer. Consequently, the three final depth slices were set to 0–0.36 m (topsoil), 0.36 m–0.86 m (highest subsoil EC variability) and below 0.86 m (deeper subsoil layers).

The three resulting EC^* maps are given in Fig. 5. EC_1^* (Fig. 5a) shows that, whereas the topsoil (0–0.36 m) mainly contains noise, the EC_2^* map (0.36–0.86 m) (Fig. 5b) amplifies the subsoil variability in the measurements. Compared to the four individual ECa measurements (Fig. 3), the range of the EC_2^* values is larger, resulting in more distinct conductivity differences between the features and the background (Fig. 5b). In the modelled EC_3^*, only a limited number of features appear, indicating that these features extend into the deeper soil layers.

6. Excavation results

A subarea of 0.85 ha was excavated down to 0.7 m (polygon on Fig. 3) and all subsoil features were digitised (Fig. 6). The meandering features proved to be small tidal creeks. The linear structures were found to be ditches, representing field boundaries and the enclosure of a medieval farmstead and farmyard (not marked on Fig. 6). Both ECa measurements and EC_2^*-depth slice were evaluated at the excavated site. $ECa_{\mathrm{PERP},2}$ (Fig. 3b) and $ECa_{\mathrm{HCP},1}$ (Fig. 3c) provided subtle indication of the ditches and the small tidal creek. However, they could be more clearly delineated based on the EC_2^* map (Fig. 5b). The continuity of both ditches and creeks could even be traced beyond the borders of the excavation zone.
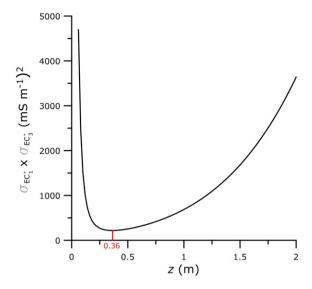

Fig. 4. $\sigma_{EC_1^*} \times \sigma_{EC_3^*}$ as the minimisation function as a function of the depth z, with indication of the optimum z of 0.36 m.

7. Verification

To compare the measured ECas and modelled ECs with field verifications, we digitised the subsoil features based on the excavation results. This verification image was classified into two classes: class 1 combined the pixels without distinct features and class 2 bundled the larger features as obtained from the excavation results. Afterwards, we stratified the four ECa-measured and three EC^*-modelled maps according to this verification image. To compare the variability in both zones, we calculated the coefficient of variation (CV), defined as ratio between the standard deviation and the mean (Table 2). A clear distinction in CV was observed: CVs of EC_2^* for both zones were considerably higher than for all ECa measurements, demonstrating that the modelled EC_2^* contains a higher variability than the ECa measurements. On the other hand, the differences in mean values between the zones were highest for EC_2^*. The differences are expressed by the relative difference (RD). For the ECa measurements and modelled EC^*s, this RD was calculated as:

$$\mathrm{RD} = \frac{X_{\mathrm{zone2}} - X_{\mathrm{zone1}}}{X_{\mathrm{zone2}}} \tag{7}$$

with X being the modelled mean EC^* or ECa measurements.

The relative difference between the zones proved to be substantially higher for the EC_2^*-depth slice, as can be seen in Table 2.

8. Evaluating discrimination potential: edge detection

Edge detection is a tool for feature detection in image processing. This technique selects pixels identifying locations where the brightness of the image changes abruptly (Accame and De Natale, 1997). So edge detection provides an objective measure to find sharp image discontinuities. Among the edge detection methods proposed, the Canny edge detector (Canny, 1986) is the most rigorously defined operator and it is widely used (Ding and Goshtasby, 2001). The Canny method identifies edges by looking for local maxima of the image gradient. The gradient is calculated using the derivative of a Gaussian filter. This method is less likely to be fooled by noise and thus able to detect weak edges.

Fig. 7 shows the results of the Canny edge detection for both $ECa_{\mathrm{PERP},2}$ and EC_2^*. $ECa_{\mathrm{PERP},2}$ was selected from the four ECa measurements as the soil volume from this coil configuration pair (DOE: 1.0 m) corresponds best to the excavation results (to a depth of 0.7 m). Furthermore, these
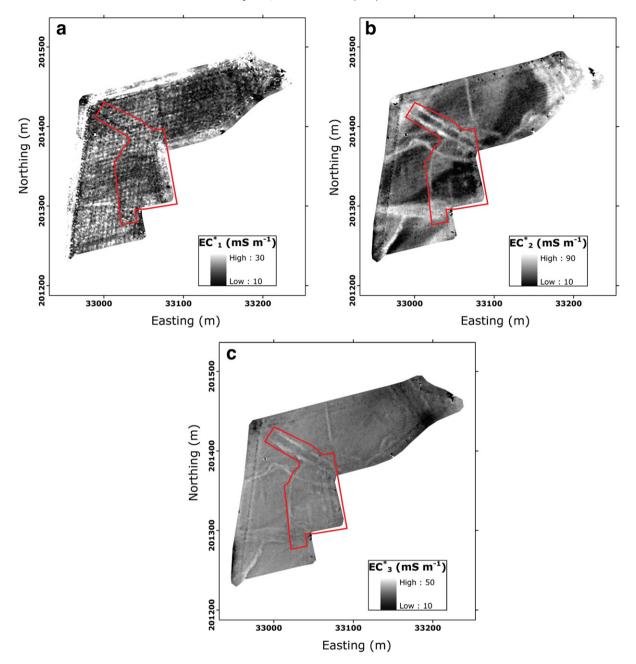
Fig. 5. Modelled conductivity map within a depth of 0 and 0.36 m (EC_1^*) (a), within 0.36 and 0.86 m (EC_2^*) (b) and below 0.86 m (EC_3^*) (c).

measurements contain the largest variability of the four ECa measurements (Table 1).

The automated Canny filter from the software package Matlab (Mathworks Inc., Massachusetts, USA) was applied to both images on Fig. 7. A two-element vector, which contains a low and high threshold, was needed for the automated filter. The high threshold was chosen to be 0.15, which implies the low threshold to be 0.06 (or 0.4×0.15). With these values, the delineated edges coincided best with the feature boundaries, deduced from the excavation results. The edge detection of the modelled EC_2^* clearly corresponds more to the excavation results than the feature boundaries found on the $ECa_{PERP,2}$ data. As such, the modelled EC_2^* clearly allows a more straightforward delineation of the subsoil features (Fig. 6). Therefore, this technique proves to be a qualitative method to recognise these contrasting subsoil features.

9. Conclusions

This study showed that the detected subsoil features could be more effectively delineated using EC-depth slicing, especially when interface depths can be identified that account for the layer with the highest EC variability. Assuming a layered earth where the layers have a constant thickness, the application of this EC-depth slicing procedure enhances the maximum horizontal conductivity gradient. This method amplifies the lateral conductivity contrasts in a specific layer, but is less suited to study the variability of the conductivity with depth. Integrating the ECas of simultaneous measurements by multiple receivers of an EMI instrument adds discriminating potential, compared to individual measurements. The more straightforward delineation of contrasting features on the EC-depth slice with the highest
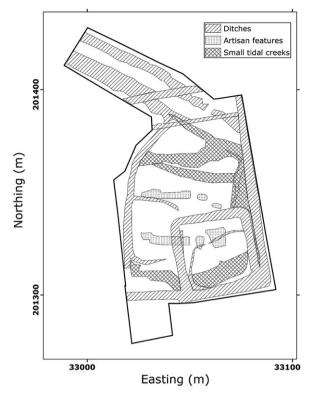
Fig. 6. Digitised map of the excavated archaeological features at a depth of 0.7 m.

variability was proven by performing an edge detection procedure. Hereby, more feature boundaries were automatically detected on the EC-depth slice with the highest conductivity contrast.

To conclude, the developed EC-depth slicing approach provides insights into the multi-receiver EMI data by enhancing the contrast between subsoil features and the background within predefined layers. This can be done for a variety of applications in order to distinguish subtle anomalies, invisible on the single sensor measurements. Moreover, this approach could be applied to reduce the effort of field soil surveys and verifications with the aim at guiding additional prospection techniques, such as excavations.

Acknowledgements

Table 2
Descriptive statistics (m: mean (mS m^{-1}), CV: coefficient of variation (%) and RD: relative difference (%)) of the four ECa measurements and modelled EC$_1$*, EC$_2$* and EC$_3$* and stratified according to the two classes of the validation image.

Variable	Class 1 (without)		Class 2 (with)		RD
	m	CV	m	CV	
ECa$_{PERP,1}$	19	21	21	15	10
ECa$_{PERP,2}$	24	21	26	15	8
ECa$_{HCP,1}$	29	16	31	12	6
ECa$_{HCP,2}$	30	12	31	10	3
EC$_1$*	20	25	21	28	5
EC$_2$*	37	52	45	38	18
EC$_3$*	31	8	30	11	3

References

Accame, M., De Natale, F.G.B., 1997. Edge detection by point classification of Canny filtered images. Signal Processing 60, 11–22.

Baeteman, C., 1991. Chronology of coastal plain development during the Holocene in West Belgium. Quaternaire 2, 116–125.

Beamish, D., 2011. Low induction number, ground conductivity meters: a correction procedure in the absence of magnetic effects. Journal of Applied Geophysics 75, 244–253.

Brosten, T.R., Day-Lewis, F.D., Schultz, G.M., Curtis, G.P., Lane, J.W., 2011. Inversion of multi-frequency electromagnetic induction data for 3D characterization of hydraulic conductivity. Journal of Applied Geophysics 73, 323–335.

Canny, J., 1986. A computational approach to edge detection. IEEE Transactions on Pattern Analysis and Machine Intelligence 8, 679–698.

Corwin, D.L., Lesch, S.M., 2005. Characterizing soil spatial variability with apparent soil electrical conductivity. Computers and Electronics in Agriculture 46, 103–133.

De Smedt, P., Saey, T., Lehouck, A., Stichelbaut, B., Meerschman, E., Islam, M.M., Van De Vijver, E., Van Meirvenne, M., 2012. Exploring the potential of multi-receiver EMI survey for geoarchaeological prospection: a 90 ha dataset. Geoderma (accepted).

Ding, L., Goshtasby, A., 2001. On the Canny edge detector. Pattern Recognition 34, 721–725.

Dualem Inc, 2007. DUALEM-21S User's Manual. Dualem Inc., Milton, Canada.

Ervynck, A., Baeteman, C., Demiddelde, H., Hollevoet, Y., Pieters, M., Schelvis, J., Tys, D., Van Strydonck, M., Verhaege, F., 1999. Human occupation because of a regression, or the cause of a transgression? A critical review of the interaction between geological events and human occupation in the Belgian coastal plan during the first millenium AD. Probleme der Küstenforschung im südlichen Nordseegebied 26, 97–121.

Goovaerts, P., 1997. Geostatistics for Natural Resources Evaluation. Oxford University Press, New York USA.

Lee, B.D., Jenkinson, B.J., Doolittle, J.A., Taylor, R.S., Tuttle, J.W., 2006. Electrical conductivity of a failed septic system soil absorption field. Vadose Zone Journal 5, 757–763.

Lehouck, A., 2010. Het verdwenen landschap en de etymologie van Koksijde. Een landschapshistorische benadering op basis van plaatsnamen. In: De Caluwe, J., Van Keymeulen, J. (Eds.), Voor Magda, Artikelen voor Magda Devos bij haar afscheid van de Universiteit Gent. Academia Press, Gent, pp. 397–419.

Marquardt, D., 1963. An algorithm for least-squares estimation of nonlinear parameters. SIAM Journal on Applied Mathematics 11, 431–441.

Martinelli, H.P., Robledo, F.E., Osella, A.M., de la Vega, M., 2012. Assessment of the distortions caused by a pipe and an excavation in the electric and electromagnetic responses of a hydrocarbon-contaminated soil. Journal of Applied Geophysics 77, 21–29.

McNeill, J.D., 1980. Electromagnetic terrain conductivity measurement at low induction numbers. Technical Note TN-6, Geonics Limited. Missisauga, Ontario, Canada.

Monteiro Santos, F.A., Triantafilis, J., Bruzgulis, K.E., Roeb, J.A.E., 2010. Inversion of multiconfiguration electromagnetic (DUALEM-421) profiling data using a one-dimensional laterally constrained algorithm. Vadose Zone Journal 9, 117–125.

Pellerin, L., Wannamaker, P.E., 2005. Multi-dimensional electromagnetic modeling and inversion with application to near-surface earth investigations. Computers and Electronics in Agriculture 46, 71–102.

Robinson, D., Abdu, H., Lebron, I., Jones, S., 2012. Imaging of hill-slope soil moisture wetting patterns in a semi-arid oak savanna catchment using time-lapse electromagnetic induction. Journal of Hydrology 416–417, 39–49.

Saey, T., Simpson, D., Vermeersch, H., Cockx, L., Van Meirvenne, M., 2009a. Comparing the EM38DD and DUALEM-21S sensors for depth-to-clay mapping. Soil Science Society of America Journal 73, 7–12.

Saey, T., Van Meirvenne, M., Vermeersch, H., Ameloot, N., Cockx, L., 2009b. A pedotransfer function to evaluate the soil profile textural heterogeneity using proximally sensed apparent electrical conductivity. Geoderma 150, 389–395.

Saey, T., De Smedt, P., Meerschman, E., Islam, M.M., Meeuws, F., Van De Vijver, E., Lehouck, A., Van Meirvenne, M., 2011a. Electrical conductivity depth modelling with a multireceiver EMI sensor for prospecting archaeological features. Archaeological Prospection, http://dx.doi.org/10.1002/arp. 425 (published online).

Saey, T., Van Meirvenne, M., Dewilde, M., Wyffels, F., De Smedt, P., Meerschman, E., Islam, M.M., Meeuws, F., Cockx, L., 2011b. Combining multiple signals of an electromagnetic induction sensor to prospect land for metal objects. Near Surface Geophysics 9, 309–317.

Tromp-van Meerveld, H.J., McDonnell, J.J., 2009. Assessment of multi-frequency electromagnetic induction for determining soil moisture patterns at the hillslope scale. Journal of Hydrology 368, 56–67.

Vandenbohede, A., Lebbe, L., 2011. Groundwater chemistry patterns in the phreatic aquifer of the central Belgian coastal plain. Applied Geochemistry, http://dx.doi.org/10.1016/j.apgeochem.2011.08.012.

Vitharana, U.W.A., Saey, T., Cockx, L., Simpson, D., Vermeersch, H., Van Meirvenne, M., 2008. Upgrading a 1/20,000 soil map with an apparent electrical conductivity survey. Geoderma 148, 107–112.

Wait, J.R., 1962. A note on the electromagnetic response of a stratified earth. Geophysics 27, 382–385.

Webster, R., Oliver, M.A., 2007. Geostatistics for Environmental Scientists, Second edition. John Wiley & Sons, Chichester.
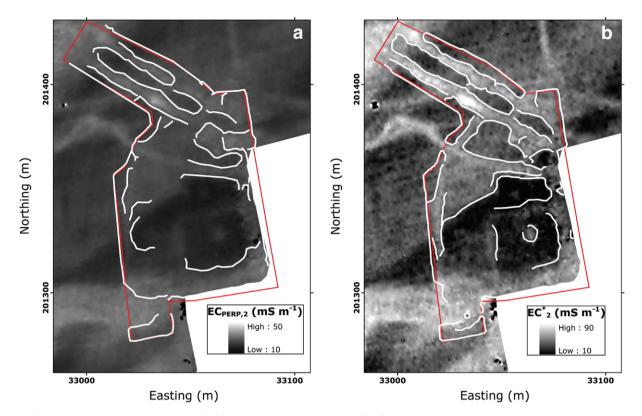
Fig. 7. Measured ECa$_{PERP,2}$ and modelled EC$_2^*$ of the excavated site, with indication of the feature delineations based on the edge detection algorithm.